Front. Earth Sci. 2016, 10(1): 135–144
DOI 10.1007/s11707-015-0487-6

RESEARCH ARTICLE

Source analysis of spaceborne microwave radiometer interference over land

Li GUAN (✉), Sibo ZHANG

Collaborative Innovation Center on Forecast and Evaluation of Meteorological Disasters, Key Laboratory for Aerosol-Cloud-Precipitation of China Meteorological Administration, Nanjing University of Information Science & Technology, Nanjing 210044, China

Abstract Satellite microwave thermal emissions mixed with signals from active sensors are referred to as radio-frequency interference (RFI). Based on Advanced Microwave Scanning Radiometer–Earth Observing System (AMSR-E) observations from June 1 to 16, 2011, RFI over Europe was identified and analyzed using the modified principal component analysis algorithm in this paper. The X band AMSR-E measurements in England and Italy are mostly affected by the stable, persistent, active microwave transmitters on the surface, while the RFI source of other European countries is the interference of the reflected geostationary TV satellite downlink signals to the measurements of spaceborne microwave radiometers. The locations and intensities of the RFI induced by the geostationary TV and communication satellites changed with time within the observed period. The observations of spaceborne microwave radiometers in ascending portions of orbits are usually interfered with over European land, while no RFI was detected in descending passes. The RFI locations and intensities from the reflection of downlink radiation are highly dependent upon the relative geometry between the geostationary satellite and the measuring passive sensor. Only these fields of view of a spaceborne instrument whose scan azimuths are close to the azimuth relative to the geostationary satellite are likely to be affected by RFI.

Keywords AMSR-E, RFI, geostationary TV satellite

1 Introduction

During the past several decades, many spaceborne microwave radiometers have been launched into space. Low-frequency microwave observations are mainly used for obtaining information about soil moisture (Owe et al., 2001), vegetation water content, surface temperature (Njoku et al., 2003, 2005), and snow cover (Kelly et al., 2003). Today C- and X-band frequencies (6.9 GHz and 10.7 GHz, respectively) have been occupied and used for both passive and active remote sensing. The C- and X-bands of passive spaceborne microwave radiometers operate in unprotected frequency bands. These satellite measurements of the Earth's natural, thermal emission can easily be affected by the signals from lower frequency, active microwave transmitters including radar, air traffic control signals, cell phone, garage door remote controls, highway GPS signals, defense tracking, vehicle speed detection by law enforcement, etc. Such a phenomenon of satellite-measured passive microwave thermal emission being mixed with the signals from active sensors is referred to as radio-frequency interference (RFI) (Zou et al., 2012). In recent years, due to the increasing conflict between scientific and commercial users of the radio spectrum, RFI has become a serious problem for microwave radiometry. A series of Special Sensor Microwave/Imager (SSM/I) instruments (Hollinger et al., 1990), the Advanced Microwave Scanning Radiometer–EOS (AMSR-E) onboard the National Aeronautics and Space Administration (NASA) Earth Observing System (EOS) Aqua satellite in 2002 (Kawanishi et al., 2003), the WindSat radiometer on the Department of Defense Coriolis satellite in 2003 (Gaiser et al., 2004; Ellingson and Johnson, 2006), the MicroWave Radiation Imager (MWRI) onboard the second-generation Chinese polar-orbiting satellite FY-3B in 2010 (Zhang et al., 2009) and FY-3C in 2013, and the successor of AMSR-E, AMSR-2 onboard the Global Change Observation Mission 1st-Water (GCOM-W1) satellite in 2012 all include X-band or both C- and X-band channels to enhance surface sensing capabilities. The RFI problem poses a significant challenge to current microwave missions and will remain a serious issue for

Received February 9, 2014; accepted July 21, 2014

E-mail: liguan.nuist@gmail.com

planned future projects. A software processing solution must be derived to identify and remove RFI. It is important to carry out RFI detection before these observations are delivered to users for either data assimilation or product retrievals.

If not properly identified and rejected, these RFI contaminated data could significantly reduce the scientific value of existing and future C- and X-band passive microwave missions (Yang et al., 2011). To this end, several methods have been developed to locate the RFI and quantify its magnitude. Existing methods for various sensors include the spectral difference method, the mean and standard deviation method, the principle component analysis (PCA) method, the normalized PCA (NPCA) method, the double PCA (DPCA) method, and so on.

The spectral difference RFI detection technique is based on the distinct signature differences between natural radiation and RFI induced by human activities. Because the RFI has narrower bandwidth relative to natural radiation, its emission and scattering characteristics are very different, resulting in a negative spectral gradient. Li et al. (2004) proposed an RFI Index (RI) (differences between brightness temperatures at two neighboring frequencies for a given polarization) to identify the location of RFI and quantify its intensity. Moderate and strong RFI could be detected if the RI exceeded a threshold (5 K) beyond its natural variation. Such a spectral difference technique was applied only to detect ground RFI in summer; it was not optimal for ocean RFI due to inherent, large, natural variability of the spectral difference over the ocean. Based on examining the spatial and temporal characteristics of the RFI by the use of spectral indices, Njoku et al. (2005) elaborated that using means and standard deviations of the spectral indices was effective in identifying strong RFI. In principle, RFI identification relies on two kinds of information. The first is the emission and scattering characteristics represented by RIs, which is the physical information determined by the Earth's materials and by the structures of the natural targets. The second is the correlations between different channels or indices, which are the statistical information introduced by the natural variability of the targets. The multichannel correlations of radiometer data from natural radiations are often high, while the channel correlations between an RFI contaminated channel and the remaining channels are low since RFI only increases brightness temperatures significantly at a particular frequency. In over land situations, Li et al. (2006) advised the use of principal component analysis (PCA) of RIs, which integrated statistics of target emissions and scattering characteristics (through RIs) and multivariate correlation of radiometer data into a single statistical framework. It decomposed multichannel data into a number of orthonormal components according to their correlations and separated RFI components from natural variations more efficiently and consistently. However, neither the spectral difference and the PCA method could detect RFI reliably over frozen grounds and scattering surfaces in winter. To avoid taking snow and ice as false RFI signals from the aforementioned indices, Zou suggested using a normalized PCA (NPCA) method in winter (Zou et al., 2012). The RIs need to be normalized before the principal component decomposition. Detection of RFI in spaceborne microwave radiometer observations is difficult under snow- and ice-covered conditions. Zhao proposed a double PCA (DPCA) method to identify RFI over Greenland and the Antarctic (Zhao et al., 2013). The DPCA method developed for global RFI detection consisted of two PCA steps. In the first step, a vector composed of ten brightness temperatures (except for the 89 GHz) was defined for analysis. The data matrix could finally be reconstructed using the principle component coefficients in two parts, a correlated matrix and a residual matrix, where the RFI signals are contained in the residual matrix. The second step of the DPCA method was to apply a normalized PCA to the residual matrix. This method worked well not only in the non-scattering regions, but also in the scattering regions, especially for those high latitude areas covered by year-round snow or ice.

Adams et al. (2010) identified the ocean-reflected RFI using WindSat geophysical retrieval chi-square probability (goodness-of-fit) estimates, and pointed out that the interference over oceans came mainly from the reflected geostationary communication and television satellites downlink signals. Are the reflected signals emanating from geostationary television satellites the interference sources to the passive spaceborne microwave observations over land? To answer the question, the AMSR-E measurements were taken as an example to search the main radio-frequency interference source over European land in our study. This paper is organized as follows: Section 2 provides a brief description of AMSR-E data. Section 3 introduces a new modified PCA RFI detection method in detail. Numerical examples and the RFI source analysis over European land are presented in Section 4. Section 5 gives some conclusions.

2 AMSR-E Data

The AMSR-E is onboard NASA's Earth Observing System (EOS) Aqua satellite which was launched on 4 May 2002 with equator crossings at 1:30 pm and 1:30 am local time. The instrument is primarily designed to enhance cloud and surface sensing capabilities. AMSR-E has vertical and horizontal polarization channels at six frequencies, 6.925 GHz, 10.65 GHz, 18.7 GHz, 23.8 GHz, 36.5 GHz, and 89.0 GHz, for a total of 12 channels. The AMSR-E has a fixed earth incidence angle of 55°, scans conically about the nadir axis, and provides an observation swath-width of 1,445 km. The spatial resolution of the individual measurement decreases from 5.4 km at 89 GHz to 56 km at 6.9 GHz (Wu et al., 2011).

The AMSR-E Level 1A instrument data are provided by the Japan Aerospace Exploration Agency (JAXA). The Level 2A brightness temperatures are standard operational products generated by reconstructing the AMSR-E antenna gain patterns at each channel to five footprints at the Remote Sensing Systems (RSS) facility in Santa Rosa, CA. Hence, there are five different resolutions for the re-sampled data from 56 to 5.4 km. Four channels will be used in our study to calibrate spectral difference indices. Other higher frequency brightness temperature data are degraded and co-registered to the resolution of the 6.9 GHz. This ensures that brightness temperatures observed at different frequencies are referenced to approximately the same spatial surface area. For the Level 2A data, if the measured brightness temperature of one channel exceeds 330 K, the observations are all set to zero (Njoku et al., 2005). The FOVs with zero value observations are represented by some small white areas in the figures of brightness temperature. AMSR-E Level 2A observations from June 1 to 16, 2011 are used in this paper and Europe is selected as the research area.

3 The modified PCA (MPCA) RFI detection method

The brightness temperatures of natural surfaces tend to increase with the frequency at frequencies below 30 GHz, so RI is negative in that frequency range. However, RFI can increase brightness temperatures significantly at a contaminated frequency, and therefore generate a positive RI. When volume scattering effects dominate over snow-covered surfaces, the brightness temperatures reduce with increases in frequency, so the RI values over snow areas are also positive. Consequently, it is difficult to detect RFI in areas of partial snow coverage.

For describing the low-frequency scattering characteristics, the brightness temperatures (TB) at 18 GHz and 36 GHz are used to define the Scattering Index ($SI = TB_{18} - TB_{36}$) in numerous previous researches (Grody and Basist, 1996; Kelly et al., 2003). SI with high positive value denotes radiation from scattering surfaces. The MPCA method takes advantage of the multi-channel correlation for natural surface radiation including snow, as well as the decorrelation between RFI frequencies with other channels. There are three variables constructing the vector in our modified PCA method: an RFI index (RI), and two scattering indices (SI). The RI variable is sensitive to RFI contamination and the SIs are snow-sensitive.

For identifying RFI at 10.7 GHz, a vector of three-components is defined as follows:

$$\overrightarrow{RFI}_{\text{indicies}} = \begin{pmatrix} \mathrm{RI}_{10\mathrm{H(V)}} \\ \mathrm{SI_V} \\ \mathrm{SI_H} \end{pmatrix} = \begin{pmatrix} \mathrm{TB}_{10\mathrm{H(V)}} - \mathrm{TB}_{18\mathrm{H(V)}} \\ \mathrm{TB}_{18\mathrm{V}} - \mathrm{TB}_{36\mathrm{V}} \\ \mathrm{TB}_{18\mathrm{H}} - \mathrm{TB}_{36\mathrm{H}} \end{pmatrix}, \quad (1)$$

where TB denotes brightness temperature, the subscript H stands for horizontal polarization ,the subscript V stands for vertical polarization, and the subscript coefficient represent frequency.

The data matrix for identifying RFI at 10.7 GHz horizontal polarization is defined as follows:

$$\boldsymbol{A}_{3\times N} = \begin{pmatrix} (\mathrm{TB}_{10\mathrm{H}} - \mathrm{TB}_{18\mathrm{H}})_1 & (\mathrm{TB}_{10\mathrm{H}} - \mathrm{TB}_{18\mathrm{H}})_2 & \cdots & (\mathrm{TB}_{10\mathrm{H}} - \mathrm{TB}_{18\mathrm{H}})_N \\ (\mathrm{TB}_{18\mathrm{V}} - \mathrm{TB}_{36\mathrm{V}})_1 & (\mathrm{TB}_{18\mathrm{V}} - \mathrm{TB}_{36\mathrm{V}})_2 & \cdots & (\mathrm{TB}_{18\mathrm{V}} - \mathrm{TB}_{36\mathrm{V}})_N \\ (\mathrm{TB}_{18\mathrm{H}} - \mathrm{TB}_{36\mathrm{H}})_1 & (\mathrm{TB}_{18\mathrm{H}} - \mathrm{TB}_{36\mathrm{H}})_2 & \cdots & (\mathrm{TB}_{18\mathrm{H}} - \mathrm{TB}_{36\mathrm{H}})_N \end{pmatrix}, \quad (2)$$

where N is the total number of data points over a specified region.

The data matrix $\boldsymbol{A}$ can be projected onto a new orthonormal data space as shown below:

$$\boldsymbol{Z}_{3\times N} = \boldsymbol{u}^{\mathrm{T}}\boldsymbol{A} = \begin{pmatrix} Z_1 \\ Z_2 \\ Z_3 \end{pmatrix}, \quad (3)$$

Where $\boldsymbol{u}$ is eigenvector ($\boldsymbol{u} = [u_1, u_2, u_3]$). The elements of Z are often defined as the principal components which are uncorrelated to each other (Lattin et al., 2003). Each principal component (e.g., Z_1, Z_2) is an exact linear combination (i.e., weighted sum) of the original variables (e.g., RI, SI). The first principal component Z_1 exhibits maximum variance, and the second principal component Z_2 accounts for the remaining maximum variance not already accounted for by Z_1 (Jolliffe, 1976). In our data matrix, the first principal component Z_1 tends to describe the similarities of the original data set while the second and third ones lean to represent the lack of correlation.

Based on the fact that multichannel correlations of radiometric data from natural radiation are often high but decrease between the RFI low-frequency channels, 6.8 or 10.7 GHz, with the remaining AMSR-E channels, the RFI-related principal component is extracted for RFI detection. The RFI-related principal component has a higher correlation and contribution to the original RI. The higher the value of the RFI-related principal component is, the greater the probability the data are contaminated by RFI signals. A more detailed description of the MPCA method can be found in reference (Zhang and Guan, 2013).

Compared to the PCA method proposed by Li et al. (2006), our MPCA method saves computer time. The vector for analysis is simplified, including only three variables, as opposed to seven or nine variables by the PCA method. The dimensions of the data matrix are decreased greatly, so the calculation of the covariance matrix, eigenvalues, eigenvectors, and the principal components is faster. It takes just several seconds of one AMSR-E orbit to do the analysis via the MPCA method. Another key difference from other PCA methods is that the principal component with higher correlation and contribution to the original RFI index is used as the RFI-related principal component for RFI identification, while the PCA-identified RFI signal always appears in the first principal component by previous PCA methods.

4 The analysis of RFI source over European land

The AMSR-E onboard the polar-orbiting Aqua satellite covers the same areas every 16 days. Within the period of 16 days, the AMSR-E orbit swath covers slightly different areas each day. RFI distributions at 10.7 GHz with horizontal polarization over European land from 1 to 16 June, 2011 based on AMSR-E ascending observations are displayed in Fig. 1. The number in the figure denotes the date of observation. The RFI is identified using the modified principal component analysis algorithm which has been introduced in detail in above section. In all the figures of this paper, gray lines indicate the swath boundary of each orbit, and the blank zones between two intersected gray lines are the observation gap areas. As this study focuses only on RFI detected over land, a coastline mask has been applied to remove ocean and large inland water regions. Based on outside research, the threshold to identifying the RFI signal is also set to 5 K (Li et al., 2004; Wu and Weng, 2011). The areas with values exceeding the threshold are recognized as potential locations of RFI. In a second 16 day interval, the AMSR-E orbit coverage was identical to the first 16-day interval, and the locations and magnitudes of RFI were similar to Fig. 1.

In Fig. 1, the RFI distribution in England and Italy did not change with the time of observation each day, and with the magnitude being nearly constant. This result suggests that the sources of this kind of interference primarily focus on terrestrial, active emitters in the microwave region. The RFI signals in England and Italy typically originate from a wide variety of coherent point target sources, being isolated in space and persistent in time.

The recognized RFI locations in other European countries (in yellow and red color) are different every day, and the RFI intensity also changes with time. For example, the wide and strong RFI are observed in France on 2, 4, 11, and 13 June, and the RFI signals are not detected on other days within this period. The instrument orbit coverage areas of these four RFI days are nearly same. It is just the slight difference in scanning swath that leads to the difference in RFI location and intensity. Geographical areas of RFI shifting with respect to the scan location suggests a fixed, directional source. Why do RFIs in these regions change with observation time and satellite orbit, and what is the source of this kind of interference? To solve these problems, several observation areas are selected in our study. The research boxes are shown in Fig. 2 (number in box is the date of observation).

According to Adams' research, the signals emanating from geostationary communication and television satellites that reflect off the ocean surface are the major interference sources of spaceborne passive microwave imagers over the ocean (Adams et al., 2010). When wind speeds are light, the specular reflection usually happens over the ocean. The possibility is for geostationary satellite RFI to show up in descending passes and for no RFI to be detected in ascending passes in the Northern Hemisphere. However, RFI occurs in ascending passes in the Southern Hemisphere (Adams et al., 2010). The current major geostationary television satellites are listed in Table 1. The TV satellites effecting Europe are Hot Bird, Atlantic Bird, and Astra, all with emitting frequencies concentrated at 10.7 GHz. Direct TV satellites, with a frequency of 18.7 GHz, broadcast to the US (Chelle et al., 2010). Figure 3 shows the sketch map of AMSR-E observation affected by the reflected geostationary TV satellite downlink signals. The contour lines in blue color denote the coverage and power of geostationary TV satellite downlink signals. RFI from the reflections of downlink radiation off the ocean surface are highly dependent upon the relative geometry between the geostationary satellite and the measuring passive sensor, and these interfering signals exhibit an angular spread due to non-specular reflection. RFI occurs only when the RFI glint angle is smaller than 25° over the ocean. The angle between the space-borne radiometer line-of-sight vector and the specular reflection vector is defined as glint angle.

Based on the RFI analysis over Europe using AMSR-E observations within the 16-day period in Fig. 1, we primarily conclude that the geostationary TV satellites' radiation reflecting off the land surface and into the field-of-view of space-borne microwave radiometers will also interfere with passive Earth observations. The RFI affected regions vary with time, and depend on scan position and line-of-sight vector. Geographical areas of RFI shifting with respect to the location within the scan suggests a fixed, directional source. Due to the heterogeneity of land, the reflections over land are mostly non-specular reflections. In Fig. 1, geostationary satellite RFI shows up in AMSR-E ascending passes over Europe, while no RFI is detected in descending passes. The result is opposite to that found over the ocean surface.

Geostationary communication and television satellites maintain fixed positions above the Earth's equator and

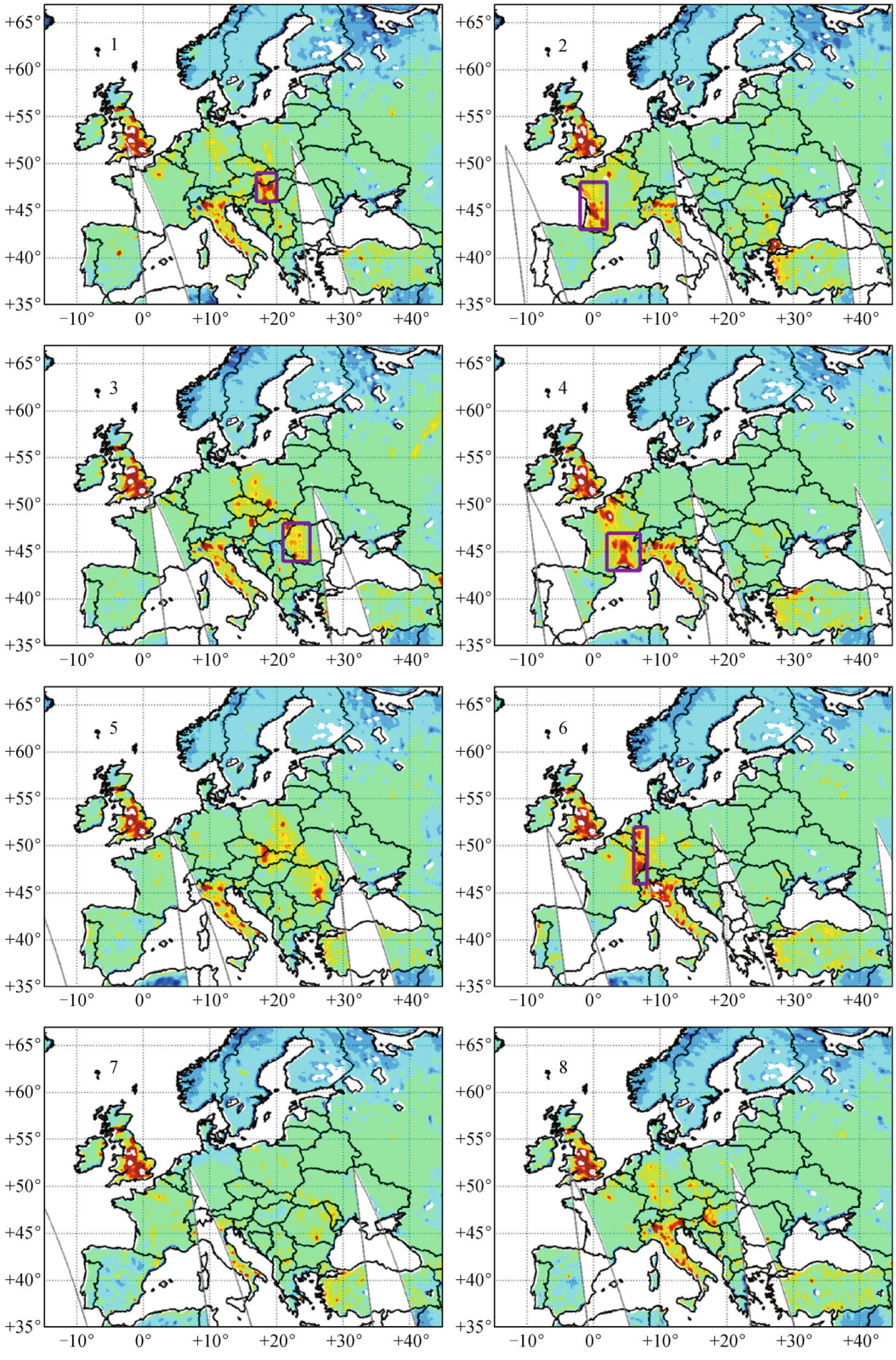
1
2
3
4
5
6
7
8
+65°
+60°
+55°
+50°
+45°
+40°
+35°
−10°
0°
+10°
+20°
+30°
+40°

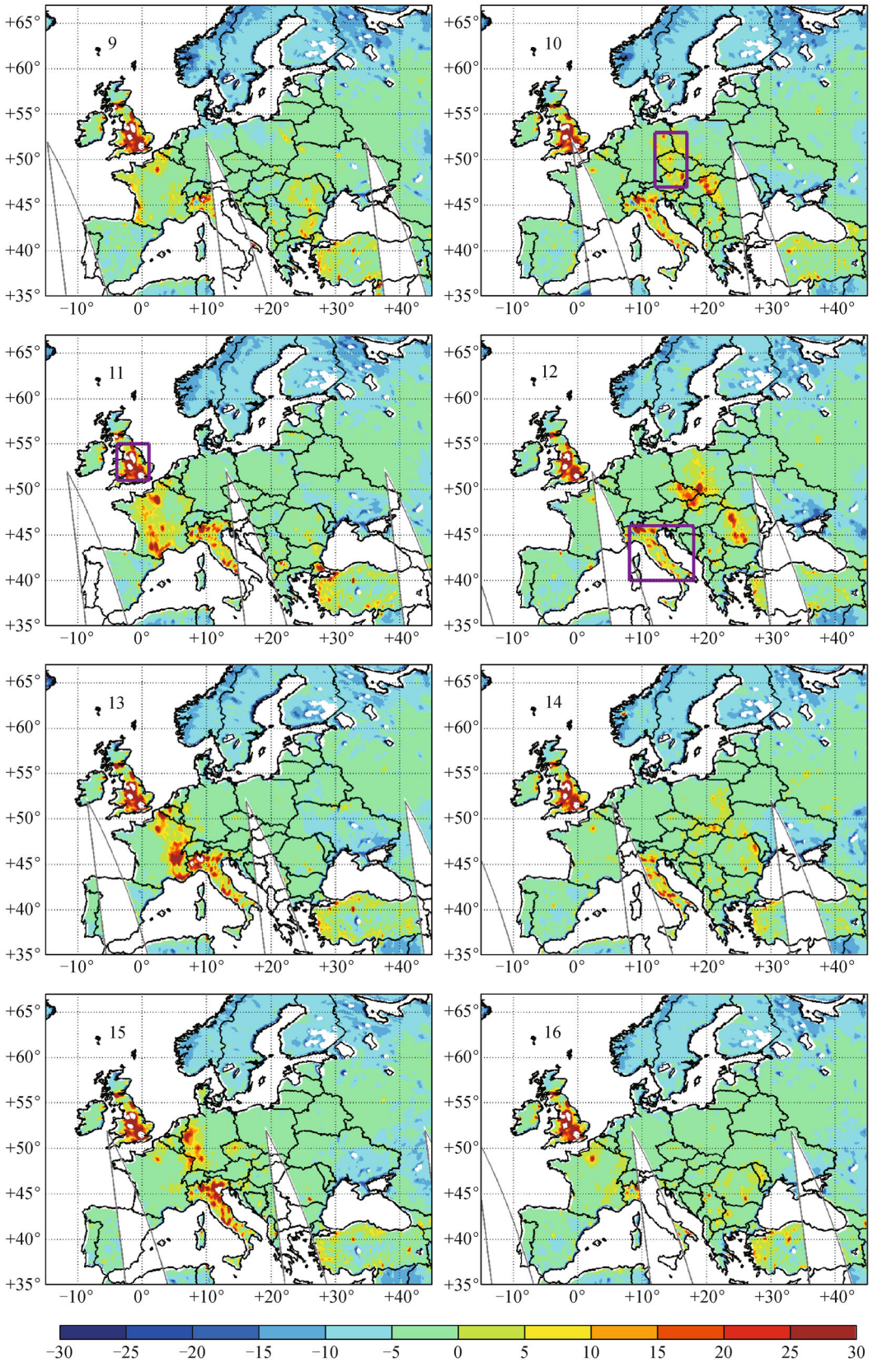

Fig. 1 RFI distributions at 10.7 GHz with horizontal polarization over Europe from 1 to 16 June, 2011 based on AMSR-E ascending observations (numbers in figure denote dates).

Table 1 Major geostationary TV satellite

Operator	Longitude degrees	Region	Relevant Band /GHz
DirecTV 10	103°W	USA	19.3–18.8
DirectV 11	99°W	USA	18.3–18.8
Atlantic Bird	7°W	Europe	10.7–11.7
Hot Bird	13°E	Europe	10.7–12.75
Astra	19.2°E	Europe	10.7–10.95

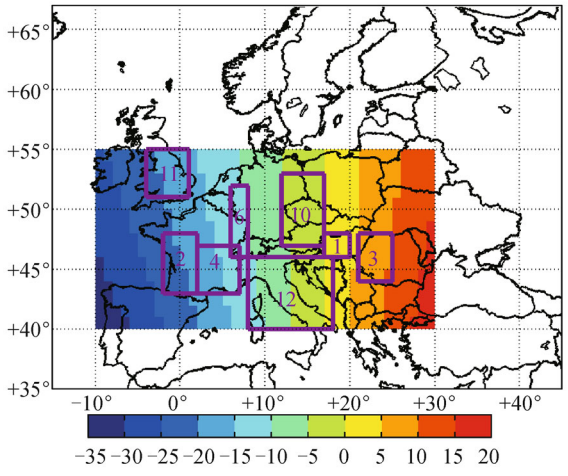

Fig. 2 Box locations are the research areas for Fig. 1 (number in box is the observation date). Color contours denote the averaged downlink azimuth of geostationary satellites Astra and Hot Bird.

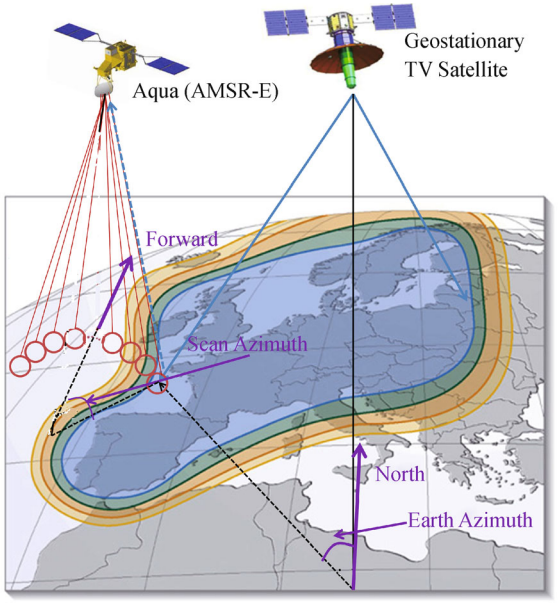

Fig. 3 The sketch map of AMSR-E observations affected by the reflected, geostationary TV satellite downlink signals.

constantly transmit to predetermined regions. The antenna patterns for European geostationary satellites are designed to focus transmissions only to designated regions in the Northern Hemisphere. The color contour in Fig. 2, displays the downlink azimuth relative to the geostationary satellite. The azimuth denotes the angle between the projected geostationary satellite downlink viewing vector and the north-oriented vector at the observation point. Clockwise is positive and anticlockwise is negative. Because the energy beam of Atlantic Bird is mainly projected to the ocean and the energy beams of geostationary satellites Astra and Hot Bird are focused over European land, the average downlink azimuth of geostationary satellites Astra and Hot Bird are shown as the color shaded area in Fig. 2.

AMSR-E is a conically scanning instrument that provides the earth azimuth variable in its Level2A data. It is the angle between the north-oriented vector and the projected line-of-sight vector at the observation point. Again, clockwise is positive and anticlockwise is negative. AMSR-E views the Earth across arcs in the forward direction relative to the satellite forward motion vector, so the earth azimuth ranges [−90° 90°]. To study the relationship between the RFI location and the AMSR-E scan azimuth, we define the scan azimuth as the angle between the satellite-flying vector and the projected line-of-sight vector. Scanning to the left is negative and to the right is positive. Because the orbit inclination of the Aqua satellite is 98.3°, the difference between scan azimuth and earth azimuth is 8.3°.

The relationships between instrument scan azimuth and the recognized RFI using the modified PCA method in eight selected research areas are shown in Fig. 4. The locations and dates of the eight selected research boxes are shown in Fig.2. The AMSR-E scan azimuth is displayed on the vertical axis; the RFI magnitude is displayed on the horizontal axis. Box11 and Box12 cover England and Italy respectively. The distributions and magnitudes of RFI in these two areas do not change with scan azimuth; strong RFI interference can always be detected. This further validates that the RFI sources in these two countries are persistent, stable active emitters on the land surface; the reflected geostationary satellite influence is less important. In the other study boxes, not every field of view is affected by reflected, geostationary satellite signals. RFI from the

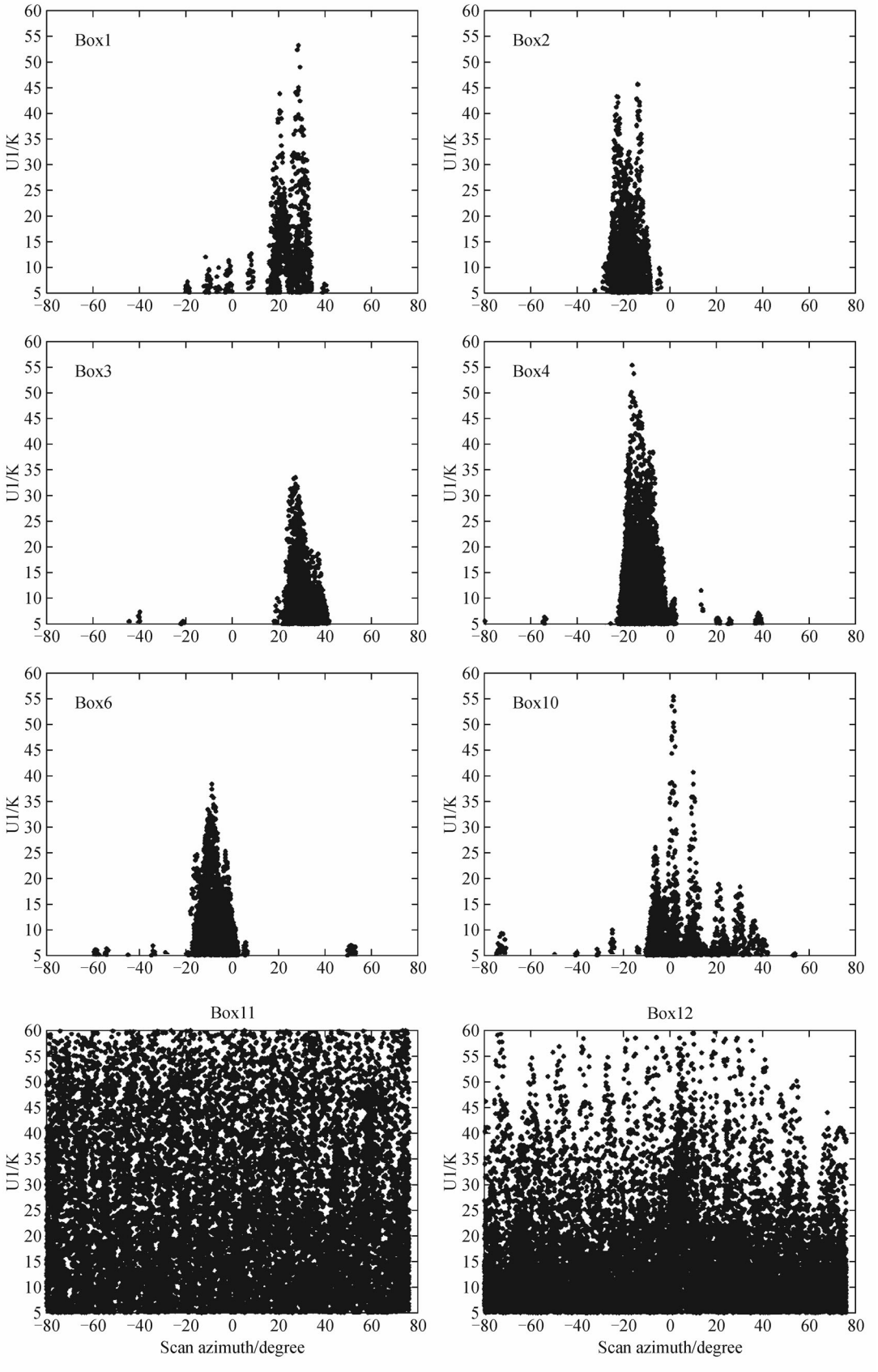

Fig. 4 The relationship between RFI intensity (horizontal axis) and AMSR-E scan azimuth (vertical axis) in research areas.

reflections of downlink radiation off the surface are highly dependent upon the relative geometry between the geostationary satellite and the measuring passive sensor. The affected region depends on the scan position and the line-of-sight vector. Only these fields of view which scan azimuths within a certain range are affected by RFI.

Let us analyze the information contained in Box2, Box4, and Box6 in detail. In Fig. 2, the azimuth angles of the geostationary satellite downlink radiation are all negative in these 3 boxes, meaning these areas are to the left of the geostationary satellite. The AMSR-E scan azimuths of the RFI fields of view in Fig. 4 are in ranges $[-25-10]$, $[-20-5]$ and $[-15-5]$ in Box2, Box4, and Box6, respectively. The observed scan azimuth angles are all negative, which denotes the RFI appears to the left of the satellite flying direction. With the location of Box6, Box4, and Box2 further westward to the geostationary satellite in Fig. 2, the corresponding scan azimuths of RFI fields of view distribute further leftward relative to the satellite flying direction in Fig. 4. The fields of view affected by RFI from the reflections of downlink radiation off the surface depend on scan azimuth (scan position) of the spaceborne radiometer and its azimuth angle relative to geostationary satellite downlink. The fact that Box1 and Box3 are located to the east of the azimuth of the geostationary satellite accords with that the scan azimuth of these RFI fields of view within these boxes in Fig. 4 are all positive. The RFI scan azimuths within Box3 located easterly to the geostationary satellite are more rightward. The azimuth angles relative to the geostationary satellite downlink shown in Box10 are close to zero so the RFI is focused on a nadir scan.

The location of the RFI is highly dependent upon the relative geometry between the geostationary satellite and the measuring passive sensor. RFI appears in the leftward scan points relative to flying direction when fields of view are located to the west of the azimuth of the geostationary satellite. Conversely, RFI appears in the rightward scan points relative to flying direction when fields of view are located to the east of the azimuth of the geostationary satellite. The comparison of the average azimuth of the research boxes relative to the geostationary satellite in Fig. 2 with the scan azimuth of these fields of view affected by RFI in Fig. 4 demonstrates that the values of these two azimuth angles are very close. Only the field of view of a spaceborne microwave radiometer whose scan angle is close to the azimuth relative to the geostationary satellite downlink is likely to be affected by RFI.

5 Conclusions

Radio-frequency interference at X-band over Europe is identified and analyzed based on AMSR-E observations from June 1 to 16, 2011 using the modified principal component analysis algorithm in this paper. This newly developed RFI identification method works well in detecting the location and intensity of RFI over Europe. It performs well not only over non-scattering surface in summer but also over scattering surface in winter.

Except for in England and Italy, the RFI locations and intensities in other European countries change with time periodically. The signals emanating from geostationary communication and television satellites that reflect off the land surface are the major interference sources of these RFI. Geostationary satellite RFI shows up in AMSR-E ascending passes over Europe, while no RFI is detected in descending passes.

The location of the RFI is highly dependent upon the relative geometry between the geostationary satellite and the measuring passive sensor. RFIs appear in the leftward scan points relative to flying direction when fields of view are located to the west azimuth of the geostationary satellite. Conversely, RFIs appear in the rightward scan points relative to flying direction when fields of view are located to the east azimuth of the geostationary satellite. Only these fields of view of a spaceborne microwave radiometer whose scan angles are close to the azimuth relative to the geostationary satellite downlink are likely to be affected by RFI. Geographical areas of RFI shifting with respect to the location within the AMSR-E scan suggests a fixed, directional pollution source. The RFI distribution with this characteristic can be considered primarily to come from the interference of geostationary satellites. Next step, the geopgraphical distribution of RFI from geostationary satellites over ocean will be analyzed.

Acknowledgements This work was jointly supported by the National Natural Science Foundation of China (Grant No. 41175034) and Key University Science Research Project of Jiangsu Province (No. 13KJA170003).

References

Adams I S, Bettenhaused M H, Gaiser P W, Johnston W (2010). Identification of ocean-reflected radio-frequency interference using WindSat retrieval Chi-Square probability. IEEE Geosci Remote Sens Lett, 7(2): 406–410

Chelle G, Marty B, Kyle H (2010). Algorithm development GCOM-W AMSR-2 ocean product suite, Joint PI Workshop of Global Environment Observation Mission, Tokyo, Japan

Ellingson S W, Johnson J T (2006). A polarimetric survey of radio-frequency interference in C- and X-Bands in the continental United States using WindSat Radiometry. IEEE Trans Geosci Rem Sens, 44 (3): 540–548

Gaiser P W, St Germain K M, Twarog E M, Poe G A, Purday W, Richardson D, Grossman W, Jones W L, Spencer D, Golba G, Cleveland J, Choy L, Bevilacqua R M, Chang P S (2004). The WindSat spaceborne polarimetric microwave radiometer: sensor description and early orbit performance. IEEE Trans Geosci Rem Sens, 42(11): 2347–2361

Grody N C, Basist A N (1996). Global identification of snowcover using SSM/I measurements. IEEE Trans Geosci Rem Sens, 34(1): 237–249

Hollinger J P, Peirce J L, Poe G A (1990). SSM/I instrument evaluation. IEEE Trans Geosci Rem Sens, 28(5): 781–790

Jolliffe I T (1976). Principal Component Analysis. New York: Springer-Hill

Kawanishi T, Sezai T, Ito Y, Imaoka K, Takeshima T, Ishido Y, Shibata A, Miura M, Inahata H, Spencer R W (2003). The advanced microwave scanning radiometer for the earth observation system (AMSR-E), NASDA's contribution to the EOS for global enery and water cycle studies. IEEE Trans Geosci Rem Sens, 41(2): 184–194

Kelly R E, Chang A T, Tsang L, Foster J L (2003). A prototype AMSR-E global snow area and snow depth algorithm. IEEE Trans Geosci Rem Sens, 41(2): 230–242

Lattin J M, Carroll J D, Green P E (2003). Analyzing Multivariate Data. Beijing: China Machine Press, 83–123

Li L, Gaiser P W, Bettenhausen M H, Johnston W (2006). WindSat radio-frequency interference signature and its identification over land and ocean. IEEE Trans Geosci Rem Sens, 44(3): 530–539

Li L, Njoku E G, Im E, Chang P S, St Germain K S (2004). A preliminary survey of radio-frequency interference over the U. S. in aqua AMSR-E data. IEEE Trans Geosci Rem Sens, 42(2): 380–390

Njoku E G, Ashcroft P, Chan T K, Li L (2005). Global survey and statistics of radio-frequency interference in AMSR-E land observations. IEEE Trans Geosci Rem Sens, 43(5): 938–947

Njoku E G, Jackson T J, Lakshmi V, Chan T K, Nghiem S V (2003). Soil moisture retrieval from AMSR-E. IEEE Trans Geosci Rem Sens, 41 (2): 215–229

Owe M, de Jeu R, Walker J (2001). A methodology for surface soil moisture and vegetation optical depth retrieval using the microwave polarization difference index. IEEE Trans Geosci Rem Sens, 39(8): 1643–1654

Wu Y, Weng F (2011). Detection and correction of AMSR-E radio-frequency interference. Acta Meteorologica Sinica, 25(5): 669–681

Zhang P, Yang J, Dong C, Lu N, Yang Z, Shi J (2009). General introduction on payloads, ground segment and data application of Fengyun 3A. Front Earth Sci China, 3(3): 367–373

Zhang S, Guan L (2013). Identifying AMSR-E Radio-Frequency Interference over Snow Covered Land. Frontiers of Earth Science (revised).

Zhao J, Zou X, Weng F (2013). WindSat radio-frequency interference signature and its identification over greenland and antarctic. IEEE Trans Geosci Rem Sens, 51(9): 4830–4839

Zou X, Zhao J, Weng F, Qin Z (2012). Detection of radio-frequency interference signal over land from FY-3B microwave radiation imager (MWRI). IEEE Trans Geosci Rem Sens, 50(12): 4994–5003